FEBS Letters 586 (2012) 4208–4214

journal homepage: www.FEBSLetters.org

# Signaling regulated endocytosis and exocytosis lead to mating pheromone concentration dependent morphologies in yeast

Ching-Shan Chou [a,*,1], Travis I. Moore [b,c,1], Steven D. Chang [c,1], Qing Nie [b,d], Tau-Mu Yi [b,c,e]

[a] Department of Mathematics, The Ohio State University, Columbus, OH 43210, USA
[b] Center for Complex Biological Systems, University of California at Irvine, Irvine, CA 92697, USA
[c] Department of Developmental and Cell Biology, University of California at Irvine, Irvine, CA 92697, USA
[d] Department of Mathematics, University of California at Irvine, Irvine, CA 92697, USA
[e] Department of Molecular, Cellular, and Developmental Biology, University of California at Santa Barbara, Santa Barbara, CA 93106, USA

ARTICLE INFO

*Article history:*
Received 28 August 2012
Revised 1 October 2012
Accepted 14 October 2012
Available online 27 October 2012

Edited by Francesc Posas

*Keywords:*
Yeast mating
Cell polarization
Cell morphology
Deforming membrane
Membrane dynamics
Signaling mediated endocytosis

ABSTRACT

**Polarized cell morphogenesis requires actin cytoskeleton rearrangement for polarized transport of proteins, organelles and secretory vesicles, which fundamentally underlies cell differentiation and behavior. During yeast mating, *Saccharomyces cerevisiae* responds to extracellular pheromone gradients by extending polarized projections, which are likely maintained through vesicle transport to (exocytosis) and from (endocytosis) the membrane. We experimentally demonstrate that the projection morphology is pheromone concentration-dependent, and propose the underlying mechanism through mathematical modeling. The inclusion of membrane flux and dynamically evolving cell boundary into our yeast mating signaling model shows good agreement with experimental measurements, and provides a plausible explanation for pheromone-induced cell morphology.**


## 1. Introduction

Cells respond to internal and external cues by selectively permitting growth in specific regions of the cell membrane to achieve non-spherical shapes [1]. Studies have found that the actin cytoskeleton, a major target of signaling events, undergoes rearrangement and mediates transport of proteins, organelles and secretory vesicles toward sites of growth, giving rise to polarized morphogenesis ([2,3], reviewed in [4,5]).

In morphogenesis of yeast and mammalian cells, the organization of the actin cytoskeleton and vesicle transport along a vectorial axis requires an intricate regulation orchestrated by active G-proteins, Cdc42p and other GTPases, to control the establishment of polarity [3,6,7]. Activation of Cdc42p leads to a localized recruitment of actin cables and actin patches at the site of Cdc42p accumulation on the cell membrane; however, the details of the pathways linking Cdc42p to actin polymerization are still unclear [8].

Since morphogenesis requires sustained assembly of actin cables, the maintenance of Cdc42p polarization and other cortical proteins is crucial. Three general schemes have been invoked to explain such polarization [4]: (1) a preexisting stably polarized "anchor" interacts with a protein of interest, thereby increasing its concentration; for example, in yeast budding, "bud site selection" proteins are deposited at the cell poles during bud formation, allowing them to serve as "landmarks" that bind anchor proteins in subsequent cell cycles [9]; (2) a diffusion barrier is established that prevents protein diffusion between compartments; in budding yeast, septin filament systems act as a diffusion barrier during budding; (3) dynamic control through polarized delivery and endocytic retrieval of cortical proteins to sites of polarization thereby limiting the length scale of lateral membrane diffusion. In yeast mating projection (shmoo) formation, a morphogenesis process in which no evident diffusion barrier has been found (although the septin structure at the base of the projection may potentially act in this manner), endocytosis and exocytosis could play critical roles in both maintaining polarity and expanding the membrane to produce the projection, if the proteins and vesicles are kinetically recycled and fuse with the native membrane, leading to a change in the total area of cell membrane.

In experiments of *Saccharomyces cerevisiae* exposed to differential mating pheromone concentrations, different cell morphologies were observed. At high pheromone concentrations, mating projections are observed to be thinner and shorter than those exposed to

* Corresponding author. Address: 412 Math Tower, 231 West 18th Ave., Columbus, OH 43210, USA.
*E-mail address:* chou@math.osu.edu (C.-S. Chou).
[1] These authors contributed equally to this work.

0014-5793/$36.00 
http://dx.doi.org/10.1016/j.febslet.2012.10.024

lower pheromone concentrations. Previous studies suggest that endocytosis is a receptor-mediated process where binding of extracellular ligand by the extracellular portion of transmembrane receptors facilitates heterotrimeric G-protein activation and internalization of the receptor–ligand complex [10], and exocytosis regulated by the intracellular signaling of Cdc42p [11]. This evidence leads us to propose that differential cell morphologies in response to ligand concentration are a result of the balance between endocytosis and exocytosis, in other words, a balance between G-protein and Cdc42p signaling.

An efficient way to test this hypothesis is to develop a mathematical model that incorporates the signaling transduction pathway and permits deformation of the cell membrane. A number of mathematical models have been developed to investigate dynamics of actin filaments in cell morphogenesis [12,13]. Different aspects of actin dynamics, such as the actin monomer cycle and actin polymerization at the leading cell edge [14], and roles of vesicle trafficking on signaling and polarization [15,16], are inspected in various models. Fluid-based models are also used to simulate the motion or deformation of eukaryotic cells [17–19]. Level set approaches coupled with the associated biochemistry are used to approximate the deforming cell membrane [20–22].

In this paper, we propose a mathematical model that couples the signaling pathway and the deforming cell membrane. We will first introduce a single-module model to demonstrate the capability of the model to generate budding and mating projections morphologies in yeast cells. Then we will explain the pheromone dependent experimental data by using a two-module model of Gβγ (G-protein) and Cdc42p signaling, whose levels correlate with levels of endocytosis and exocytosis. It is important to note that this division of labor between heterotrimeric G-protein and Cdc42 is a model hypothesis (and simplification) that needs to be tested and refined by further experiments. Nevertheless, numerical simulations show that different balances between Gβγ and Cdc42p signaling indeed result in differential cell length and width, and the cell morphologies are consistent with the experimental results both qualitatively and quantitatively.

## 2. Materials and methods

To investigate the morphological changes induced by yeast cell polarity, we use models consisting of polarization related species, with molecular membrane diffusion, reactions, and signal amplification mechanisms described by the reaction–diffusion equations. The detailed description of the model equations, parameter selection and numerical simulations are provided in Supplementary materials. Experimental details including yeast strains, imaging and microfluidic experiments are described in Supplementary materials.

## 3. Results

### 3.1. Framework for modeling yeast cell morphological changes – a single-module model

To study the cell morphological change induced by cell polarization, we start with a simple single-module model consisting of two species $a$ and $b$, in a domain describing the cell membrane that is subject to morphological changes. The species $a$ represents a membrane associated protein undergoing polarization in response to an external or internal spatial cue, for example, Cdc42p in budding yeast. The other species $b$ represents a global negative regulator of $a$, and is uniformly distributed throughout the cell, or can be perceived as a fast diffusing species (e.g. inhibitor of Cdc42p activation). The dynamics of $a$ and $b$ are governed by a reaction–diffusion system, Eqs. (1) and (2), in which the lateral surface diffusion, cooperative production, positive feedback and degradation of $a$ are included, while $b$ regulates $a$ through an integral feedback loop. The details of how each term models molecular mechanisms are described in Supplementary materials.

$$\frac{\partial a}{\partial t} = D\nabla_m^2 a + \frac{k_0}{1+(\beta u)^{-q}} + \frac{k_1}{1+(\gamma\ pa)^{-h}} - k_2 a - k_3 b a, \tag{1}$$

$$\frac{db}{dt} = k_4(\tilde{a} - k_{ss})b, \tag{2}$$

$$\tilde{a} = \frac{\int_s a\ ds}{\int_s ds}, \quad p = \frac{1}{1+(\beta u)^{-q}}.$$

The domain of interest is the cross section of the cell membrane, which undergoes morphological changes and is essentially a closed curve of time dependent shape. With the point on the domain denoted by $\mathbf{x} = z(\xi,t)\mathbf{e}_z + r(\xi,t)\mathbf{e}_r$, where $(z,r)$ is its Cartesian coordinate parameterized by $\xi$, and $\mathbf{e}_z$ and $\mathbf{e}_r$ the corresponding unit vectors, the motion of the domain is given by

$$\frac{d\mathbf{x}}{dt} = (z_t, r_t) = V_n(\mathbf{x},t)\mathbf{n} + T(\mathbf{x},t)\mathbf{s}. \tag{3}$$

In Eq. (3), $\mathbf{n}$ is the outward normal vector of the membrane, with $V_n$ as the outward normal velocity, and $\mathbf{s}$ is the tangential direction of the membrane, with $T$ a specified tangential velocity. The motion of the cell membrane will be dictated by $V_n$, but not affected by $T$.

Biologically, the velocity of cell growth in budding yeast depends on the rate of assembly and polarized organization of actin patches and actin cables. Both are concentrated at sites of polarized growth, and actin cables are thought to mediate polarized exocytosis, which contributes to the cell growth [23,24]. Evidence has been reported that Cdc42p regulates the polarized organization of actin patches and actin cables [5,8]. In this paper, we directly associate the growth velocity $V_n$ with the concentration of Cdc42p ($a$), although other players may also be involved in the cell growth. Thus, $V_n$ is a function of $a$, and Eqs. (1)–(3) form a closed system describing the spatial dynamics of the proteins and the deforming domain. The details of the numerical simulation are provided in the Supplementary materials.

In yeast cells, budding and mating projection formation require cell polarization and share many downstream structural and signaling pathways, yet each process results in dramatically different morphologies. Both initially grow from the tip; however, budding becomes isotropic midway while the shmoo retains a constant pointing tip growth toward the source of stimulation [25,26]. In this section, we demonstrate the capability of the single-module model to capture both yeast morphologies using different parameters and, more importantly, different functions of velocity in Eq. (3).

Budding is initiated by a remnant cortical cue from the previous budding event that can be considered as an input, and represented by the spatially dependent function $u$ in the equation. This internal cue induces polarization of proteins, such as Bud5 and Rsrl, which in turn transmits the signal downstream inducing the polarization of Cdc42 and other proteins. This first recruitment stage can be modeled as the cooperativity $k_0$ term in Eq. (1). It has been shown that Bem1 recruitment forms a positive feedback loop of Cdc42 recruitment and activation, corresponding to the positive feedback $k_1$ term in Eq. (1). Inhibition of this Cdc42 activation has been shown to be mediated by Cla4 and is simply modeled as $b$ in Eq. (2), reviewed in [27].

We started exploring how those distinct morphologies can be obtained by characterizing the normal velocity $V_n(\mathbf{x},t)$. Simulations revealed that when $V_n(\mathbf{x},t)$ is proportional to $a$, a growing bud can

be successfully reproduced, Fig. 1A. Since the current model is a simplistic model created to demonstrate the moving boundary framework methodology, many details are omitted. In particular, we did not consider the bud neck formation or the septin mediated diffusion barrier in budding. Inclusion of additional pathway elements would be required to achieve a continual bud formation that pinches off from the mother.

A pheromone gradient serves as the input for mating projection formation, which is transduced through membrane receptors. This binding event can be modeled through the cooperativity $k_0$ term. The Cdc42 positive feedback loop, as in the budding, is mediated by Bem1 and Cdc24, and inhibited by Cla4. The simplistic model captures the basic spatial dynamics of cell polarization, as verified by the mass action model in [28]. The polarisome, which directs cytoskeleton dynamics and projection shape, is more tightly localized than its upstream activator Cdc42. Therefore, we model the velocity of the cell membrane to be $[k(\mathbf{n}\cdot\mathbf{d_L})a]\mathbf{n}$, where $k$ is a constant, taken as 0.02, and $\mathbf{d_L}$ is the unit vector along the direction of the external gradient. The appearance of $\mathbf{n}\cdot\mathbf{d_L}$ is to model the fact that the cytoskeleton of localized and pointing to the tip of the shmoo. As a result, the simulation reproduces the shmoo shape as in Fig. 1B.

Altogether, by defining the velocity functions in biologically relevant terms we can replicate cellular morphology using our single-module model. In the following sections we will show a greater understanding of cell morphology dynamics through the incorporation of additional signaling pathway components into the velocity functions.

### 3.2. Yeast mating projection morphologies are pheromone concentration dependent

We observed that the morphology and growth rate of yeast mating projections toward α-factor pheromone gradients are dependent on the average mating factor concentration. Cells stimulated with high concentration of α-factor have thinner and shorter projections, while those in lower concentrations are wider and longer, both orient in a gradient dependent manner [29]. Fig. 2A shows the morphologies of cells treated with a range of α-factor concentrations (0, 3, 10, 30, 100 and 1000 nM) after 3 h. From the images an inverse relation between pheromone concentration and the resulting mating projection width and length can be seen.

The morphological differences of cells were quantified for systematic investigation. Measurements are defined as a comparison of cells before and after projection formation: cells imaged before and after pheromone stimulation were superimposed so the rear of the cells were aligned along the projected direction, as illustrated in Fig. 2B. The diameter of the cell pre-stimulation was measured along projection axis (length) and perpendicular to the projection axis (width). Projection width is defined as the distance between the two points where the projection extends from the unstimulated cells perimeter and post-stimulation cell length as the distance from the cell's rear to projection tip. Projection length was calculated by subtracting the pre-stimulation length from the post-stimulation length. To normalize across all cells, a ratio of the projection length or projection width and pre-stimulation cell diameter was calculated, Fig. 2C.

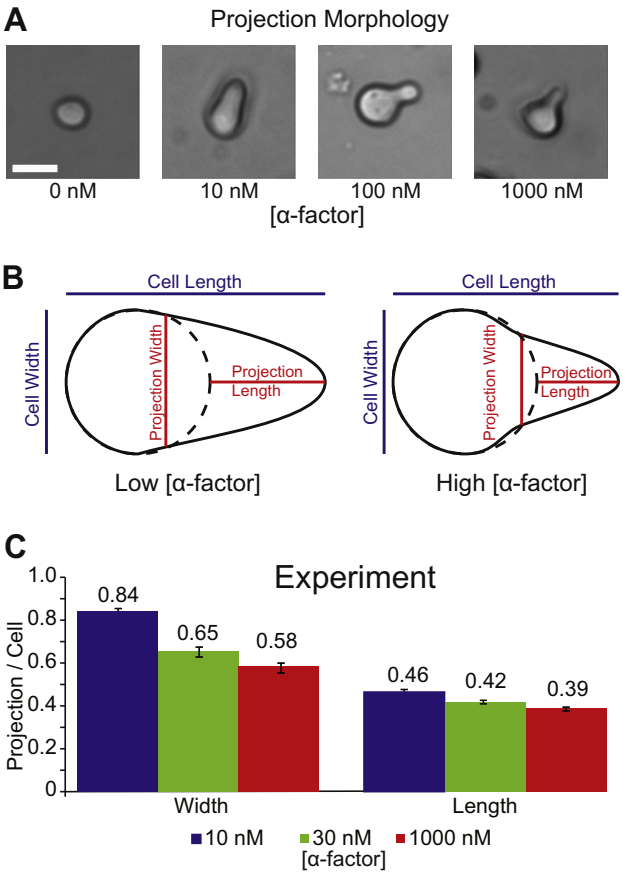


**Fig. 2.** Yeast projection width and length are inversely related to pheromone concentration. (A) Yeast cells after 3 h exposure of α-factor (0, 3, 10, 30, 100 and 1000 nM) form morphologically distinct mating projections (scale bar = 5 μm). (B) Schematic of projection length and width quantification. Projection length and width are determined by comparing cell images before and after exposure to a pheromone gradient. (C) Statistics of projection length and width normalized by pre-stimulation cell diameter are compared after exposure to high and low concentrations of α-factor (10 nM, blue bars, $n = 24$; 30 nM, green bars, $n = 24$; 1000 nM, red bars, $n = 24$; there was a significant difference between the 10 and 1000 nM data by $t$-test, $P < 0.001$).

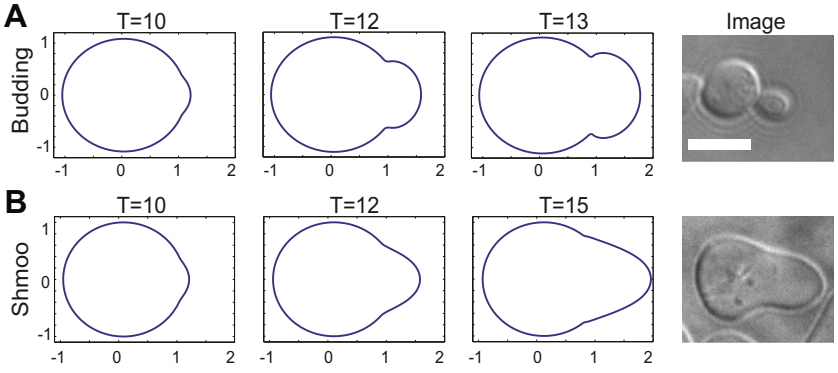


**Fig. 1.** Budding (A) and mating projection (B) morphologies simulated using the single-module model at three time points. Simulations are compared with images of cells taken during each process (scale bar = 5 μm).

Statistics were calculated on 24 cells in α-factor of high (1000 nM), medium (30 nM) and low (10 nM) concentrations, with 1 nM/μm pheromone gradients applied to both. The cell length and width were measured after 3-h exposure to α-factor. Fig. 2C shows the histograms of the experiments, with the lengths and widths scaled by the original diameters of the cell to eliminate the variation of cell sizes in the sample. The average projection widths in low pheromone concentrations are significantly greater than at high concentrations (0.84, 0.65 and 0.58, unit-less after scaling, $P < 0.001$, two-tail Student $t$-test), and the averaged length is significantly longer after exposure to low pheromone concentrations compared to high concentration (0.46, 0.42 and 0.39, $P < 0.001$, two-tail Student $t$-test). While both the length and width of the projection depend on the pheromone concentration, the measurement reveals that the difference in cell width is more pronounced. Unlike some chemotactic cells such as *Dictyostelium* and neutrophils, yeast cells are not motile. During mating the shape and overall size of yeast change significantly, and membrane surface area directly results from the flux of bi-layer lipids via vesicular trafficking, endocytosis and exocytosis. It has been reported that during mating projection formation, endocytosis and exocytosis do not take place in a uniform fashion around the cell membrane, but instead are polarized under the direction of localized signaling pathways. Therefore it is possible that the net effect of the associated signals results in the morphology of the cell, and thus is determined by the balance of the receptor and Cdc42p signaling.

We hypothesize that differential shmoo morphology is a result of this balance between receptor-mediated endocytosis (G-protein signaling) and exocytosis (Cdc42 signaling). Higher concentration of ligand results in more occupied receptors and higher Gβγ signaling. Projection growth at high concentrations occurs primarily at the tip, so we assumed that away from the tip, the endocytosis rate is approximately the same as the exocytosis rate. Since more receptors are occupied and G-protein signaling stronger, there is more endocytosis over the membrane which balances out the exocytosis. Net transport of vesicles is equivalent and focused at the tip resulting in projections that are shorter and thinner. Conversely, in cells exposed to lower concentrations of pheromone, we hypothesize that the rate of endocytosis would be reduced because there are fewer ligand-bound receptor molecules to be internalized. We tested this hypothesis by measuring the uptake of the membrane dye FM4-64 at different concentrations of α-factor: 0, 3, 10, and 100 nM (Fig. 3A). Internalization of the dye was quantitated by fluorometer (details in Supplementary materials). We found that the rate of endocytosis increased as the pheromone dose increased. Although the difference between the data at 10 and 100 nM was modest, it was consistent with the expected trend.

Therefore, at low α-factor, there will be more net transport of lipids. The hypothesized model to explain the pheromone concentration dependent shmoo differences experimentally observed is depicted in Fig. 3B.

### 3.3. Two-module model linking G-protein cycles to vesicle trafficking and morphology

To explore the influence of signaling mediated vesicular trafficking on cellular polarization and morphology, a model that incorporates both Gβγ and Cdc42p signaling cycles is required, Eqs. (4)–(7):

$$\frac{\partial a_1}{\partial t} = D\nabla_m^2 a_1 + \frac{k_{10}}{1+(\beta_1 u)^{-q_1}} + \frac{k_{11}}{1+(\gamma_1 a_1 p_1)^{-h_1}} - (k_{12}) + k_{13} b_1) a_1 \quad (4)$$

$$\frac{\partial b_1}{\partial t} = k_{14}(\tilde{a}_1 - k_{1ss}) b_1 \quad (5)$$

$$\frac{\partial a_2}{\partial t} = D\nabla_m^2 a_2 + \frac{k_{20}}{1+(\beta_2 a_1)^{-q_2}} + \frac{k_{21}}{1+(\gamma_2 a_2 p_2)^{-h_2}} - (k_{22}) + k_{23} b_2) a_2 \quad (6)$$

$$\frac{\partial b_2}{\partial t} = k_{24}(\tilde{a}_2 - k_{2ss}) b_2 \quad (7)$$

$$\tilde{a} = \frac{\int_s a_1 dS}{\int_s dS}, \quad \tilde{a}_2 = \frac{\int_s a_2\ dS}{\int_s dS}, \quad p_1 = \frac{k_{10}}{1+(\beta_1 u)^{-q_1}}, \quad p_2 = \frac{k_{20}}{1+(\beta_2 a_1)^{-q_2}}$$

This model consists of two modules, both based on the structure of the single-module model (1) and (2). The Gβγ cycle is described in the first module, Eqs. (4) and (5), with its input the spatial gradient of α-factor denoted by $u$ and its output the Gβγ signaling ($a_i$). The Cdc42p cycle, constituting the second module Eqs. (6) and (7), is downstream of the Gβγ cycle ($a_1$), which is the input, and the level of activated Cdc42p ($a_2$) the output. Although the mating pathway is far more complicated and consists of many more signaling species, this two-module model captures the main structure of the two cycles related to endocytosis and exocytosis, which directly contributes to cell morphological change.

The motion of the cell membrane remains described by Eq. (3). Based on our hypothesis, the local normal velocity $V_n$ results from the net transport of vesicles through endocytosis and exocytosis, and therefore we assume that its magnitude is the net difference of exocytosis rate ($f_{EXO}$) and endocytosis rate ($f_{ENDO}$), which takes the form of Eq. (8):

$$V_n(\mathbf{x}, t) = (f_{EXO} - f_{ENDO})\mathbf{n}. \quad (8)$$

Since the endocytosis and exocytosis rate depends respectively on Gβγ and Cdc42 signaling, we model $f_{ENDO}$ as a function of $a_1$ and $f_{EXO}$ as a function of $a_2$. In Eq. (8), $f_{EXO}$ is simply taken as a linear proportion of $a_2$. As for $f_{ENDO}$, we assume that it depends on the level of Gβγ ($a_1$) as in Eq. (4): if Gβγ signaling is below a threshold $\tau$, then the endocytosis is balanced by the exocytosis, namely, $f_{ENDO} = f_{EXO}$, if the Gβγ signaling is above that threshold, the endocytosis reaches a constant saturated state. This definition ensures that the total endocytosis does not exceed exocytosis, which accounts for the total increase of the lipid on the cell membrane.

$$f_{EXO}(\mathbf{x}, t) = \rho\ a_2(\mathbf{x}, t), \quad (9)$$

$$f_{ENDO}(\mathbf{x}, t) = \begin{cases} f_{EXO}(\mathbf{x}, t), & \text{if } a_1(\mathbf{x}, t) < \tau \\ f_{EXO}(\tilde{\mathbf{x}}, t) & \text{if } a_1(\mathbf{x}, t) \geqslant \tau \end{cases} \quad \text{where } a_1(\tilde{\mathbf{x}}, t) = \tau. \quad (10)$$

The parameter $\tau$ thus determines the balance between Gβγ and Cdc42 signaling, and thereby dictates the projection shape. As $\tau$ increases, the area with a net flux of membrane lipids becomes smaller, and therefore a larger $\tau$ corresponds to the situation of higher α-factor concentration.

We first make a qualitative comparison of cell morphologies and the extent of polarization between experiments and simulations. Fig. 3C displays time-lapse images of active Cdc42 distribution visualized through the localization of its effector Ste20 tagged with GFP. The upper and lower panels correspond to experiments with 100 and 1000 nM α-factor, respectively. Within 10 min activated Cdc42 begins to localize to the front of the cell and is initially broadly distributed, Fig. 3C. Localization then becomes more focused as the projection forms and extends. In Fig. 3D it can be seen in simulations of Cdc42 ($a_2$) dynamics that higher concentration of pheromone (larger $\tau$), results in a shorter and thinner shmoo. For both high and low pheromone concentrations, Cdc42 first localizes, followed by a protrusion at the polarization site, and later Cdc42 localizes to the shmoo, encompassing almost the entire projection.

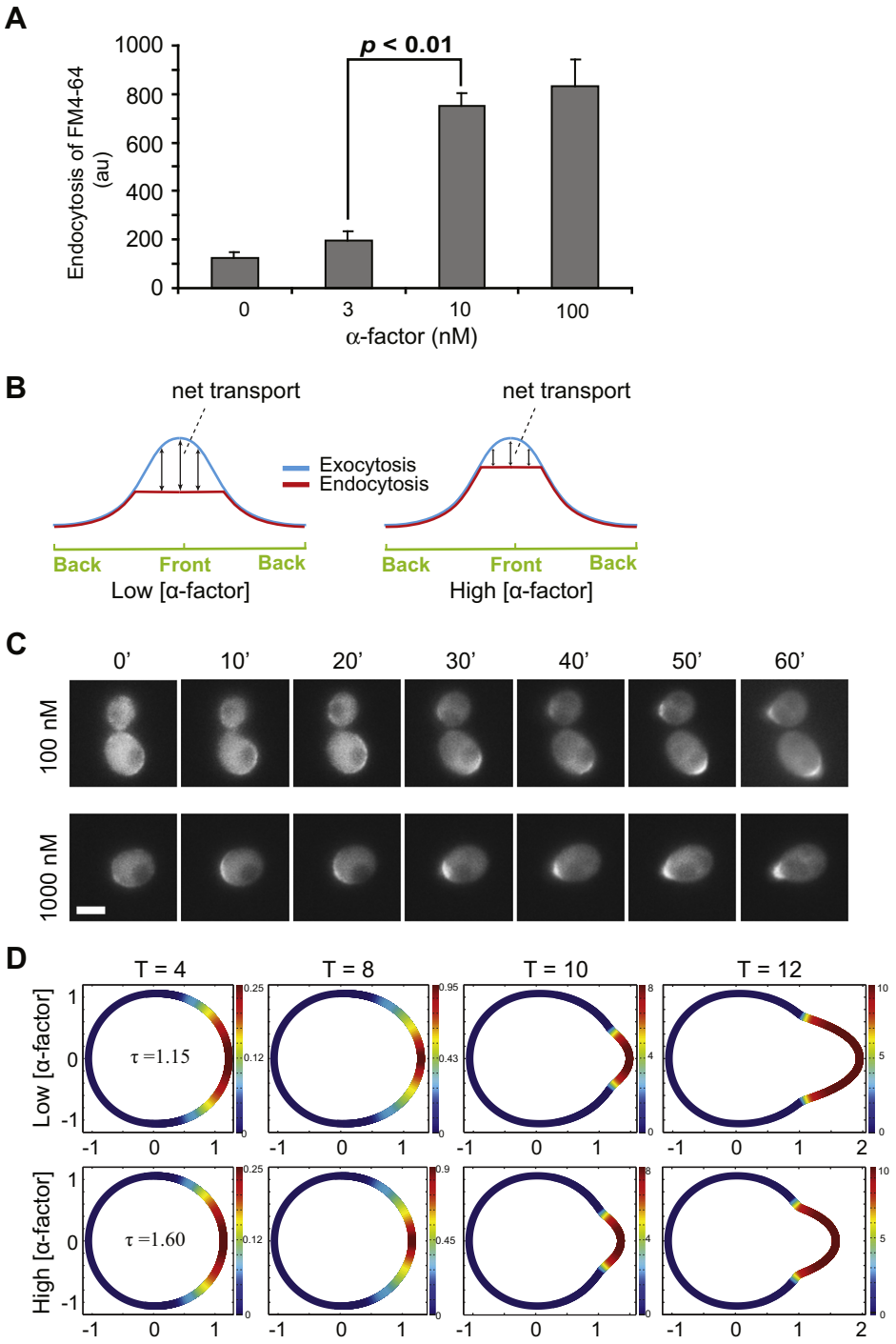


**Fig. 3.** Effect of endocytosis and exocytosis balance on cell shape. (A) Endocytosis rate as a function of α-factor dose (mean ± SEM, $n = 3$). There is a monotonic increase although only the 3–10 nM difference is statistically significant among adjacent data points. (B) Blue curves represent exocytosis level, and red curves endocytosis. The 2D cross section of the cell is represented by the ID horizontal axis, with the front of the cell (facing the highest pheromone concentration) in the middle. (C) Time-lapse images of wild-type cells containing Ste20-GFP, a marker of active Cdc42. Cells treated with isotropic α-factor pheromone, 100 and 1000 nM, for 1 h and images taken every 10 min. Over 20 cells were observed and a typical cell shown (scale bar = 2 μm). (D) Simulated Cdc42 activation levels of cells exposed to high and low pheromone concentrations, $\tau = 1.60$ and 1.15, respectively, derived from the two-module model.

These results are qualitatively consistent with the protein localization studies in Fig. 3C.

In Fig. 4A, simulated cell morphologies resulting from three values of $\tau$, can be observed: as $\tau$ decreases, the shmoo becomes wider and longer. These results, with the interpretation of $\tau$, again qualitatively agree with the observed pheromone concentration dependent morphologies in Fig. 2.

To make a quantitative comparison, one needs to define the length and width of the simulated projections. The computational framework used describes the motion of fixed tracking points on the cell membrane, making the distance between tracking points over time easily measured. We define a tracking point as fixed if its traveling distance is less than a threshold ($10^{-8}$ units). By selecting the two fixed points closest to the front of the cell

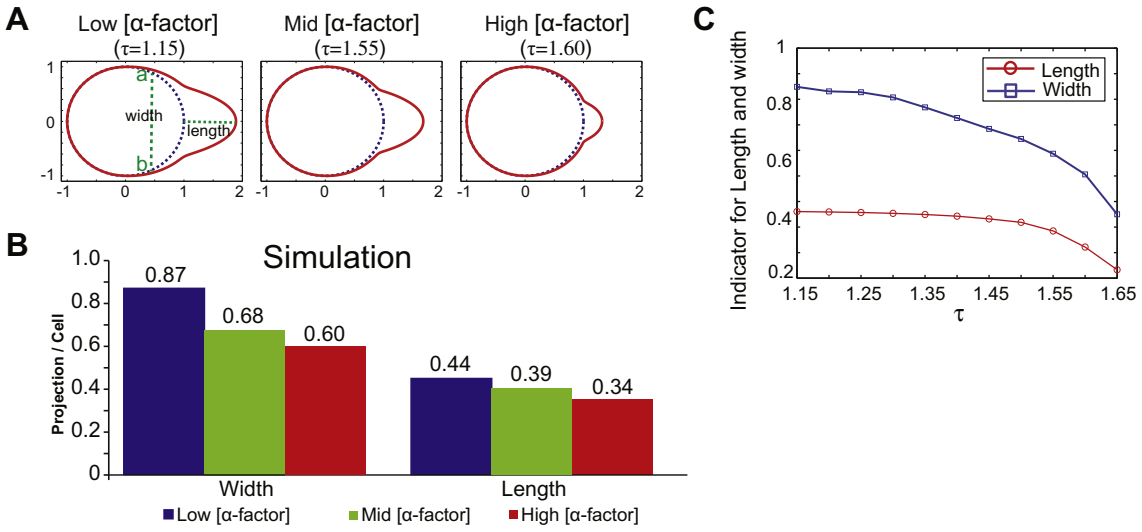


**Fig. 4.** Differential morphologies simulated by the two-module model. (A) Original cell shape, blue circles, compared with cell membrane after exposure to pheromone gradient, red curve, $T = 12$. Corresponding to low, medium, and high pheromone concentrations, cells are simulated with $\tau = 1.15, 1.55, 1.60$. Projection length is defined as the distance between the cell front at the initial and final time, and width defined as the distance between $a$ and $b$. (B) Cell width and length of simulated projections are consistent with the experimental data in Fig. 2C. Blue color represents low pheromone concentration ($\tau = 1.25$), green color medium concentration ($\tau = 1.50$) and red color high concentration ($\tau = 1.55$). (C) Inverse relation between x and cell length and width. Normalized projection length (red) and width (blue), at $T = 12$, are plotted as a function of $\tau$.

($a$ and $b$ in Fig. 4A), the width of the shmoo can be defined as the distance between $a$ and $b$, and the length of the shmoo as the distance between the front of the cell before and after projecting, represented as green dashed lines in Fig. 4A. While the threshold for defining fixed points is adjustable and could potentially affect the measurements, our extensive numerical simulations (data not shown) suggest that the length and width are not sensitive to this threshold.

With the above definition, we compare the results from three sets of parameters corresponding to low, medium and high pheromone concentrations. Due to the deterministic nature of our model, one simulation for each set of parameters is presented as a histogram, Fig. 4B, for easy comparison with experimentally derived data in Fig. 2C. In Fig. 4B, the low concentration case is marked in blue, with the width 0.87 and the length 0.44 (unit-less after scaled by the original cell diameter). The medium and high concentrations are colored in green and red respectively, with the corresponding widths 0.68 and 0.60, and the lengths 0.39 and 0.34. The data from our simulations are very close to the experimental measurements presented in Fig. 2C. The inverse relation between $\tau$ and the shmoo lengths and widths is shown in Fig. 4C.

## 4. Discussion

We have presented mathematical models that incorporate both cellular membrane signaling and deforming cell membrane of yeast cells. Modeling the deformation of the cell membrane using our single-module model, the budding and shmoo morphologies can be reproduced. Two signaling systems, heterotrimeric G-protein and Cdc42, have previously been shown to be associated with endocytosis and exocytosis and we hypothesize that their opposing influence on the membrane results in mating projection morphology. To test this theory *in silico* we developed a two-module model, based on the general framework representing G-protein and Cdc42 modules. Using the model we explain the interesting experimental observations in which mating projection morphology is affected by mating pheromone concentration. Our simulation results were shown to be quantitatively consistent with the experimental measurements, which supports our hypothesis.

This work has produced several biological insights. First, modulating the spatial dynamics of endocytosis and exocytosis can produce significantly different cell morphologies. Second, we provide modeling and experimental evidence that at higher α-factor doses, endocytosis is increased, leading to a thinner mating projection. Third, we construct a first-generation modeling framework for describing cell morphology in terms of G-protein and Cdc42 signaling and their hypothesized effect on endocytosis and exocytosis. While the change of length and width of the shmoo appears to be a nonlinear function of α-factor concentrations, further investigation is needed to determine if there is a limit of α-factor effect. Finally, future work will seek to incorporate additional physical forces that drive projection formation such as the spatial distribution of gain and loss of membrane lipid and role of actin network dynamics on vesicular trafficking, morphology, signal propagation and amplification.

## Acknowledgements

This work was supported by NIH Grants R01 GM67247 (Q.N.), P50 GM76516 (Q.N. and T.M.Y.), DMS-1001006 (T.M.Y.), NIH Training Grant in Systems Developmental Biology HD060555-01 (T.I.M.) and NSF Grants DMS-1020625 (C.S.C.), DMS-0917492 and DMS-1161621 (Q.N.).

## Appendix A. Supplementary data

Supplementary data associated with this article can be found, in the online version, at http://dx.doi.org/10.1016/j.febslet.2012.10.024.

## References

[1] Harold, F.M. (1990) To shape a cell: an inquiry into the causes of morphogenesis of microorganisms. Microbiol. Rev. 54, 381–431.
[2] Hall, A. and Nobes, C.D. (2000) Rho GTPases: molecular switches that control the organization and dynamics of the actin cytoskeleton. Philos. Trans. R. Soc. B – Biol. Sci. 355, 965–970.
[3] Wedlich-Soldner, R. and Li, R. (2004) Closing the loops: new insights into the role and regulation of actin during cell polarization. Exp. Cell Res. 301, 8–15.

[4] Irazoqui, J.E., Howell, A.S., Theesfeld, C.L. and Lew, DJ. (2005) Opposing roles for actin in Cdc42p polarization. Mol. Biol. Cell 16, 1296–1304.
[5] Slaughter, B. and Li, R. (2006) Toward a molecular interpretation of the surface stress theory for yeast morphogenesis. Curr. Opin. Cell Biol. 18, 47–53.
[6] Castellano, F., Montcourrier, P., Guillemot, J.C., Gouin, E., Machesky, L., Cossart, P. and Chavrier, P. (1999) Inducible recruitment of Cdc42 or WASP to a cell-surface receptor triggers actin polymerization and filopodium formation. Curr. Biol. 9, 351–360.
[7] Etienne-Manneville, S. (2004) Cdc42 – the centre of polarity. J. Cell Sci. 117, 1291–1300.
[8] Dong, Y., Pruyne, D. and Bretscher, A. (2003) Formin-dependent actin assembly is regulated by distinct modes of Rho signaling in yeast. J. Cell Biol. 161, 1081–1092.
[9] Schenkman, L.R., Caruso, C., Page, N. and Pringle, J.R. (2002) The role of cell cycle-regulated expression in the localization of spatial landmark proteins in yeast. J. Cell Biol. 156, 829–841.
[10] Vallier, L.G., Segall, J.E. and Snyder, M. (2002) The alpha-factor receptor C-terminus is important for mating projection formation and orientation in *Saccharomyces cerevisiae*. Cell Motil. Cytoskeleton 53, 251–266.
[11] Brennwald, P. and Rossi, G. (2007) Spatial regulation of exocytosis and cell polarity: yeast as a model for animal cells. FEBS Lett. 581, 2119–2124.
[12] Gracheva, M.E. and Othmer, H.G. (2004) A continuum model of motility in ameboid cells. Bull. Math. Biol. 66, 167–193.
[13] Maree, A., Jilkine, A., Dawes, A., Grieneisen, V. and Edelstein-Keshet, L. (2006) Polarization and movement of keratocytes: a multiscale modelling approach. Bull. Math. Biol., 1169–1211.
[14] Grimm, H.P., Verkhovsky, A.B., Mogilner, A. and Meister, J.J. (2003) Analysis of actin dynamics at the leading edge of crawling cells: implications for the shape of keratocyte lamellipodia. Eur. Biophys. J. Biophys. Lett. 32, 563–577.
[15] Birtwistle, M.R. and Kholodenko, B.N. (2009) Endocytosis and signalling: a meeting with mathematics. Mol. Oncol. 3, 308–320.
[16] Savage, N.S., Layton, A.T. and Lew, D.J. (2012) Mechanistic mathematical model of polarity in yeast. Mol. Biol. Cell 23, 1998–2013.
[17] Herant, M., Heinrich, V. and Dembo, M. (2006) Mechanics of neutrophil phagocytosis: experiments and quantitative models. J. Cell Sci. 119, 1903–1913.
[18] Rubinstein, B., Jacobson, K. and Mogilner, A. (2005) Multiscale two-dimensional modeling of a motile simple-shaped cell. Multiscale Model. Simul. 3, 413–439.
[19] Vanderlei, B., Feng, JJ. and Edelstein-Keshet, L. (2011) A computational model of cell polarization and motility coupling mechanics and biochemistry. Multiscale Model. Simul. 9, 1420–1443.
[20] Yang, L., Effler, J.C., Kutscher, B.L., Sullivan, S.E., Robinson, D.M. and Iglesias, P.A. (2008) Modeling cellular deformations using the level set formalism. BMC Syst. Biol. 2, 68.
[21] Wolgemuth, C.W. and Zajac, M. (2010) The moving boundary node method: a level set-based, finite volume algorithm with applications to cell motility. J. Comput. Phys. 229, 7287–7308.
[22] Strychalski, W., Adalsteinsson, D. and Elston, T.C. (2010) Simulating biochemical signaling networks in complex moving geometries. Siam J. Sci. Comput. 32, 3039–3070.
[23] Adams, A.E.M. and Pringle, J.R. (1984) Relationship of actin and tubulin distribution to bud growth in wild-type and morphogenetic-mutant *Saccharomyces cerevisiae*. J. Cell Biol. 98, 934–945.
[24] Karpova, T.S., McNally, J.G., Moltz, S.L. and Cooper, J.A. (1998) Assembly and function of the actin cytoskeleton of yeast: relationships between cables and patches. J. Cell Biol. 142, 1501–1517.
[25] Lew, DJ. and Reed, S.I. (1995) Cell cycle control of morphogenesis in budding yeast. Curr. Opin. Genet. Dev. 5, 17–23.
[26] Park, H.O. and Bi, E. (2007) Central roles of small GTPases in the development of cell polarity in yeast and beyond. Microbiol. Mol. Biol. Rev. 71, 48–96.
[27] Perez, P. and Rincon, S.A. (2010) Rho GTPases: regulation of cell polarity and growth in yeasts. Biochem. J. 426, 243–253.
[28] Chou, C.-S., Me, Q. and Yi, T.M. (2008) Modeling robustness tradeoffs in yeast cell polarization induced by spatial gradients. PloS One 3, e3103.
[29] Moore, T.I., Chou, C.S., Me, Q., Jeon, N.L. and Yi, T.M. (2008) Robust spatial sensing of mating pheromone gradients by yeast cells. PloS One 3, e3865.